Development and Integration of a Speed Observer for the Direct Torque Control of an Electric Propulsion System for an Electric Vehicle

João de Bruges Toledo Soares Galamba

Instituto Superior Técnico, Lisbon, Portugal

January 2021

Abstract - This paper presents the development of an adaptive speed observer for the sensorless control of a squirrel cage induction motor. Simulated results of the observer performance in are presented. The construction of a prototype PCB for the integration of the observer in the VIENA electric vehicle is also detailed.

I. Introduction

The traditional way to develop a motor's speed control uses a dedicated speed sensor. This requires a sensor to be installed on one or several of the vehicle's wheels to determine their rotational speed. This value is then converted, through the available gear ratios of the motor and transmission, into the motor's actual speed, which is then used for the control.

However, a speed sensor cannot always be installed and when this is possible, it adds complexity to the system, as well as another point of failure.

Therefore, the adoption of sensorless speed control, which leaves out additional equipment is presented. Instead, a model that takes advantage of the AC drives' extensively known characteristics is used. This model, known as a speed observer. It uses a motor's input quantities to estimate, with a high degree of accuracy, its mechanical speed, so that it can be used for control purposes.

As such, this paper proposes the development of an adaptive speed observer to be integrated in the VIENA electric vehicle

II. Theoretical Background

To develop a speed observer for this application, one must first have an understanding of the induction machine and its characteristics. This includes its dynamic performance, as the motor is part of a vehicle's powertrain, making variable-speed operation a necessity. To deal with the complexity inherent to this analysis, a two-axis *dq*-model will be used.

II.1 Induction Motor

An induction motor is an electrical machine where alternating current is directly supplied to the stator and indirectly, through induction, to the rotor.

These consist of a stator, made up of distributed windings that are mechanically displaced by 120°, and a rotor. The rotor comes in two shapes. The first, consists of distributed windings, the same as the stator. The second and most common type [1], is the squirrel cage rotor, shown in Figure 1. This consists of conducting bars, short-circuited by design at the ends, giving the rotor a cage-like appearance.
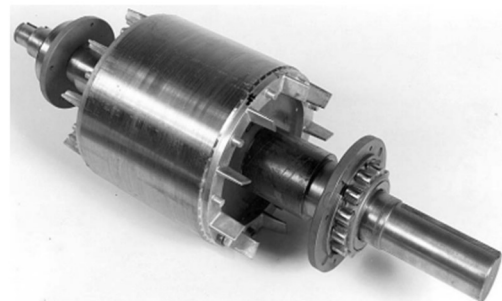

Figure 1 - Squirrel Cage Rotor of an Induction Machine (Hughes [9], p.173, Plate 5.2)

When an induction machine is powered by a balanced triphasic source, a magnetic field will be produced in the airgap rotating at a synchronous speed of N_S rpm. This speed is determined by the number of pole pairs (pp) in the machine, as well as its stator electrical frequency (f_e), as

$$N_S = \frac{60 \cdot f_e}{pp}. \qquad (1)$$

Assuming the rotor moving at a speed of N_R rpm, the difference between synchronous and rotor speed is referred to as slip (s), given by

$$s = \frac{N_S - N_R}{N_S}. \qquad (2)$$

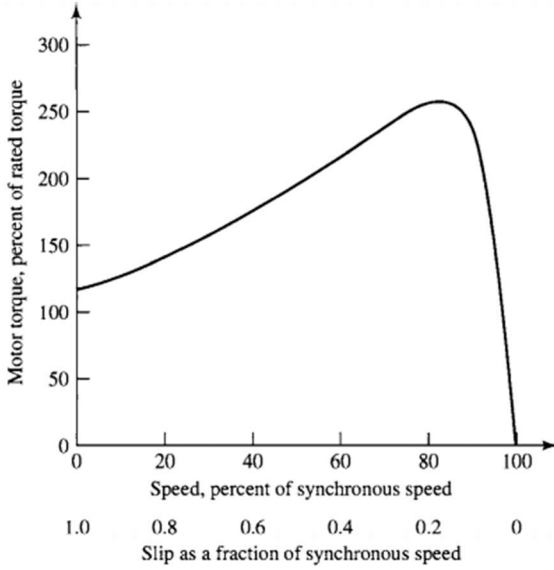A typical torque-speed curve of an induction motor can be seen in Figure 2.

Figure 2 - Typical Induction motor Torque - Speed curve (Fitzgerald [1], p.310, Figure 6.4)

Here the most important characteristic of the induction machine can be seen. The rotor speed (N_R) cannot be the same as the synchronous speed (N_S), i.e., the motor cannot operate with a slip equal to zero.

This would mean that the rotor conductors would be stationary concerning the stator field, meaning there would be no induced currents, and thus, no torque would be produced by the motor.

II.1.1 Mathematical Representation

For the mathematical representation of the induction machine some considerations must be made. Firstly, it is assumed that the motor is a 3-phase system, with a stator made of three identical windings mechanically displaced by 120°. Secondly, although the machine contains a squirrel cage rotor, this can be represented by three windings with the same arrangement as the stator.

With this in mind, the per-phase equivalent circuit, shown in Figure 3, can be created.
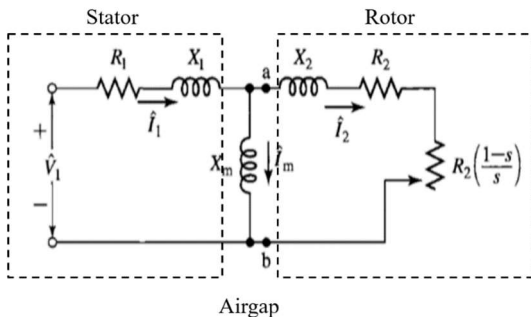

Figure 3 - Per-phase equivalent circuit of an Induction machine (Fitzgerald [1], p.319, Figure 6.11)

Here, electrical components with a similar behavior represent the physical phenomena occurring in the induction machine.

By analyzing this equivalent circuit, one is able to compute the machine's mechanical outputs, such as the power, given by

$$P_{mech} = 3R_R \left(\frac{1-s}{s} \right) I_R^2, \tag{3}$$

and the mechanical torque,

$$T_{mech} = \frac{P_{mech}}{\omega_m}, \tag{4}$$

where ω_m is the mechanical angular velocity of the rotor.

II.1.2 Scalar Command

As previously mentioned, this specific motor is used for vehicle traction, meaning variable-speed operation is necessary.

By nature, induction motors can only function efficiently near their synchronous speed, meaning speed control must provide a smooth variation of the synchronous speed. A common way to do this is to supply the motor with a variable frequency supply, using an inverter.

This is usually done while also controlling the input voltage, maintaining the ratio between frequency and voltage (V/f). This type of control can be explained with the stator voltage equation

$$V_S = R_S I_S + \frac{d\phi}{dt}. \tag{5}$$

The voltage drop in the stator can be neglected, meaning

$$V_S = R_S I_S + \frac{d\phi}{dt}, \tag{6}$$

And thus,

$$\phi \propto \frac{V}{f}. \tag{7}$$

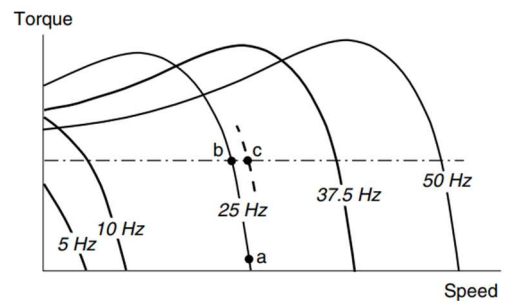This results in the family of torque-speed curves shown in Figure 4.

Figure 4 - Torque-Speed Curves with Constant V/f ratio (Hughes [9], p.286, Figure 8.3)

Here is seen how the speed can be adjusted, while maintaining enough torque to sustain the load requirements.

II.1.3   Dynamic operation

When approaching the induction machine's dynamic operation, the first component one should focus on are the machine's self and mutual inductances as they are a key part of the motor flux, described as

$$\phi = LI \tag{8}$$

Assuming a three-phase induction machine with windings on both stator and rotor, the motor inductances are given by

$$[L(\theta_{me})] \tag{9}$$
$$= \begin{bmatrix} \mathcal{L}_{aa} & \mathcal{L}_{ab} & \mathcal{L}_{ac} & \mathcal{L}_{aaR} & \mathcal{L}_{abR} & \mathcal{L}_{acR} \\ \mathcal{L}_{ba} & \mathcal{L}_{bb} & \mathcal{L}_{bc} & \mathcal{L}_{baR} & \mathcal{L}_{bbR} & \mathcal{L}_{bcR} \\ \mathcal{L}_{ca} & \mathcal{L}_{cb} & \mathcal{L}_{cc} & \mathcal{L}_{caR} & \mathcal{L}_{cbR} & \mathcal{L}_{ccR} \\ \mathcal{L}_{aRa} & \mathcal{L}_{aRb} & \mathcal{L}_{aRc} & \mathcal{L}_{aRaR} & \mathcal{L}_{aRbR} & \mathcal{L}_{aRcR} \\ \mathcal{L}_{bRa} & \mathcal{L}_{bRb} & \mathcal{L}_{bRc} & \mathcal{L}_{bRaR} & \mathcal{L}_{bRbR} & \mathcal{L}_{bRcR} \\ \mathcal{L}_{cRa} & \mathcal{L}_{cRb} & \mathcal{L}_{cRc} & \mathcal{L}_{cRaR} & \mathcal{L}_{cRbR} & \mathcal{L}_{cRcR} \end{bmatrix},$$

with (a, b, c) referring to the stator quantities and (aR, bR, cR) to the rotor quantities.

Note that the notation (θ_{me}) implies that the machine inductances are written as a function of the electrical angle between stator and rotor. This is a deciding factor, as it means that not only is the system time-dependent, because of the AC quantities, but also position-dependent, due to the mutual interactions between the inductances.

Now that the inductance matrix has been defined the three-phase stator and rotor voltage equations of the induction machine can be described as

$$[U_{abc}] = [R_{abc}][i_{abc}] + \frac{d}{dt}[\phi_{abc}], \tag{10}$$

for the stator, and

$$0 = [U_{aRbRcR}] = [R_{aRbRcR}][i_{aRbRcR}] \\ + \frac{d}{dt}[\phi_{aRbRcR}], \tag{11}$$

for the rotor. Here, the rotor voltage is zero, as the rotor coils are short-circuited by design.

II.2 dqo-Model

To simplify the computations, the Clarke and Park transformation will be used. This turns a three-phase (a, b and c), time-varying system into a two-variable, direct (d) and quadrature (q), non-time dependent system.

This is done by transforming the stator and rotor quantities into equivalent quantities that rotate at the synchronous angular velocity, meaning they are stationary to each other.

This is depicted in Figure 5, where θ_S and θ_R refer to the electrical angle between stator, rotor and the dq-

reference frame, while θ_{me} refers to the electrical angle between them.
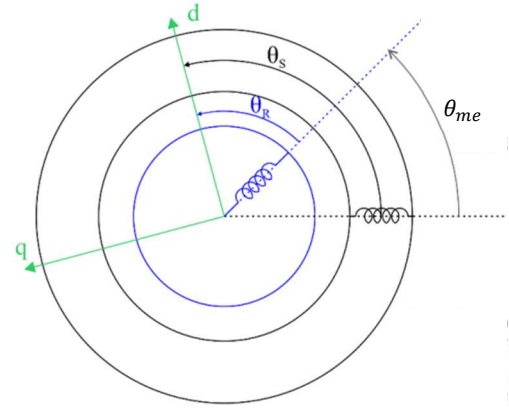

Figure 5 - Electrical angle relationship between stator, rotor and dq-reference frame

This electrical angle between stator and rotor can also be computed through the mechanical angle, θ_m, and the number of pole pairs of the machine, as

$$\theta_{me} = pp \cdot \theta_m. \tag{12}$$

II.2.1   Park Transformation

The Park transformation is used to get the machine's input voltage into the dq-reference frame, through

$$[U_{dq0}] = \frac{2}{3} \cdot [T_P] \cdot [U_{abc}], \tag{13}$$

where

$$[T_P] \tag{14}$$
$$= \begin{bmatrix} cos(\theta_S) & cos(\theta_S - \frac{2\pi}{3}) & cos(\theta_S + \frac{2\pi}{3}) \\ -sin(\theta_S) & -sin(\theta_S - \frac{2\pi}{3}) & -sin(\theta_S + \frac{2\pi}{3}) \\ \frac{1}{2} & \frac{1}{2} & \frac{1}{2} \end{bmatrix}$$

II.2.2   Induction Machine Equations

After the transformation into the dq-reference frame, the electrical equations of the induction machine can be described as following:

$$\begin{bmatrix} U_d \\ U_q \\ U_{dR} \\ U_{qR} \end{bmatrix} = \tag{15}$$
$$\begin{bmatrix} R_S & 0 & 0 & 0 \\ 0 & R_S & 0 & 0 \\ 0 & 0 & R_R & 0 \\ 0 & 0 & 0 & R_R \end{bmatrix} \begin{bmatrix} I_d \\ I_q \\ I_{dR} \\ I_{qR} \end{bmatrix} + \frac{d}{dt} \begin{bmatrix} \phi_d \\ \phi_q \\ \phi_{dR} \\ \phi_{qR} \end{bmatrix}$$
$$+ \begin{bmatrix} 0 & -\omega_s & 0 & 0 \\ \omega_s & 0 & 0 & 0 \\ 0 & 0 & 0 & -\omega_R \\ 0 & 0 & \omega_R & 0 \end{bmatrix} \begin{bmatrix} \phi_d \\ \phi_q \\ \phi_{dR} \\ \phi_{qR} \end{bmatrix}$$

with the flux, as

$$\begin{bmatrix} \phi_d \\ \phi_q \\ \phi_{dR} \\ \phi_{qR} \end{bmatrix} = \begin{bmatrix} L_S & 0 & L_M & 0 \\ 0 & L_S & 0 & L_M \\ L_M & 0 & L_R & 0 \\ 0 & L_M & 0 & L_R \end{bmatrix} \begin{bmatrix} I_d \\ I_q \\ I_{dR} \\ I_{qR} \end{bmatrix}. \qquad (16)$$

Equations 15 and 16 can then be arranged to create the state-space model of the induction machine, in the shape of

$$\frac{dx}{dt} = Ax + Bu. \qquad (17)$$

Hence,

$$\frac{d}{dt}[\phi] = [A][\phi] + [U], \qquad (18)$$

with

$$[A] = -[R][L]^{-1} - [\omega]. \qquad (19)$$

Finally, the torque equilibrium equation of the induction machine is described as

$$J_{tot}\frac{d\omega_m}{dt} = T_{el} - T_{load}, \qquad (20)$$

where

$$T_{el} = \frac{3}{2} \cdot pp \cdot \left(\phi_{dR}I_{qR} - \phi_{qR}I_{dR} \right). \qquad (21)$$

III.   Full Order State Observer

An estimator is a dynamic system whose state variables are estimates from another system, which here corresponds to an induction motor. These can be divided into two groups, open-loop or closed-loop estimators. In this case, a closed-loop estimator, also commonly referred to as an observer, will be used.

III.1   Observer Development

To develop a speed observer, the state-space model of the induction motor, seen in equation 18, is required. This model suffers a state variable change to the stator and rotor current components, as

$$\frac{d}{dt}[I] = [A][I] + [B][U], \qquad (22)$$

with

$$[A] = [L]^{-1}\left([R] + [\omega][L] \right) \qquad (23)$$

$$[B] = [L]^{-1}.$$

Now, by using the previous state-space equation (17) and implementing a term that consists of the difference between real and estimated states, i.e., the estimation error, we can implement an observer that estimates stator and rotor currents, in the form of

$$\frac{d\hat{x}}{dt} = \hat{A}\hat{x} + Bu + G\left(I_s - \hat{I}_s\right), \qquad (24)$$

Where the symbol ^ represents an estimated value, while G is an observer gain matrix that is selected so that the system is stable.

Now that the stator and rotor currents can be estimated, the system is modified to output the speed estimate of the induction machine's mechanical speed ($\hat{w}_m$). This will be done using the state-space equations (17) and (24), together with the expression for the dynamic estimation error, described as

$$e = x - \hat{x}. \qquad (25)$$

This is derived into

$$\frac{de}{dt} = \frac{dx}{dt} - \frac{d\hat{x}}{dt}. \qquad (26)$$

By replacing the terms with the results from (17) and (24), we get

$$\frac{de}{dt} = (A - GC)e - \Delta A\hat{x}, \qquad (27)$$

with

$$\Delta A = \hat{A} - A. \qquad (28)$$

Now a candidate Lyapunov function [2] in the form of

$$V = e^T e + \frac{(\hat{\omega}_m - \omega_m)}{c} \quad ; c > 0 \qquad (29)$$

is introduced. When derived, this candidate function results in

$$\frac{dV}{dt} = e\left[\frac{d(e^T)}{dt}\right] + e^T\left[\frac{de}{dt}\right] + 2\frac{d\hat{\omega}_m}{dt}\frac{(\hat{\omega}_m - \omega_m)}{c}, \qquad (30)$$

where the result from (27) can be used, resulting in

$$\frac{dV}{dt} = e^T[(A - GC)^T + (A - GC)]e - (\hat{x}^T\Delta A^T e + e^T\Delta A\hat{x}) \qquad (31)$$
$$+ 2\frac{d\hat{\omega}_m}{dt}\frac{(\hat{\omega}_m - \omega_m)}{c}.$$

Now, due to the Gain matrix [G], which is chosen so that the equation's first term is negative definite, meaning the system is stable, the following simplification can be made

$$\left(\hat{x}^T\Delta A^T e + e^T\Delta A\hat{x} \right) = 2\frac{d\hat{\omega}_m}{dt}\frac{(\hat{\omega}_m - \omega_m)}{c}. \qquad (32)$$

From here, the results from (25) and (28) are used, leading to

$$\frac{d\hat{\omega}_m}{dt} = K_I\left[Lm\left(\hat{I}_s^q e_s^d - \hat{I}_s^d e_s^q \right) + Lr\left(\hat{I}_r^q e_s^d - \hat{I}_r^d e_s^q \right) \right] \qquad (33)$$

4

Finally, a proportional gain is added to decrease the observer's response time, which gives us the equation for the estimated motor speed

$$\hat{\omega}_m = K_P\left[Lm\left(\hat{I}_s^q e_s^d - \hat{I}_s^d e_s^q\right) + Lr\left(\hat{I}_r^q e_s^d - \hat{I}_r^d e_s^q\right)\right] \quad (34)$$
$$+ \int K_I\left[Lm\left(\hat{I}_s^q e_s^d - \hat{I}_s^d e_s^q\right) + Lr\left(\hat{I}_r^q e_s^d - \hat{I}_r^d e_s^q\right)\right].$$

As for the values of the gain matrix (G), they were chosen so that the observer poles are proportional those of the induction machine [2]. This results in

$$G = -\begin{bmatrix} g_1 \cdot I_2 \cdot g_2 \cdot J \\ g_3 \cdot I_2 \cdot g_4 \cdot J \end{bmatrix} \quad (35)$$

with

$g_1 = -(k-1)\left(\frac{1}{T_S} + \frac{1}{T_R}\right)$

$g_2 = (k-1)\hat{\omega}_m$

$g_3 = (k^2 - 1)\left\{-\left[\frac{1}{T_S} + \frac{(1-\delta)}{T_R}\right] \cdot \frac{L_S L_M}{L_R} + \frac{L_M}{T_R}\right\} + L_S \frac{L_M}{L_R} \cdot (k-1) \cdot \left(\frac{1}{T_S} + \frac{1}{T_R}\right)$

$g_4 = -(k-1)\hat{\omega}_m \cdot \frac{L_S L_M}{L_R}$

and $T_S = \frac{L_S}{R_S}$, $T_R = \frac{L_R}{R_R}$ and $\delta = 1 - \frac{L_M^2}{L_S L_R}$.

Here, k, is the proportionality constant (k≥1). This parameter makes the observer faster than the induction machine but is generally kept small to reduce noise sensitivity.

III.2 Simulation

Here the output values of the simulated induction machine will be compared to those estimated by the observer, shown in Figure 6.
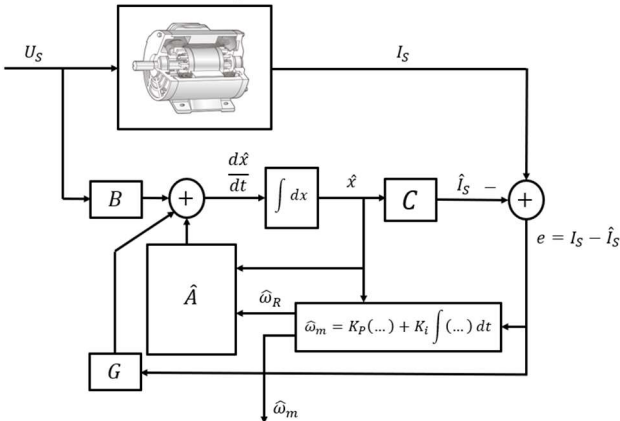

Figure 6 - Block diagram of the adaptive speed observer

Simulations will start with the simplest case, i.e., without an inverter, and progress to a scenario with an implemented inverter and V/f (scalar command).

The simulated induction motor is based on the one used in the VIENA electric car and will have a load torque of 65Nm applied to it during testing.

III.2.1 Pure Sinusoidal System

Here, the system is fed direct-on-line (DOL) with a perfect sinusoidal signal. This portrays an induction machine directly connected to its power source, without any inverter or soft starting device.

For testing the observer was configured with the values seen in Table 1, as well as resistance and inductance values that match those used in the induction motor.

Table 1 - Observer Simulation Parameters (DOL)

Observer			
k	K_I	K_P	f_{samp}
1	20000	20	10 kHz

For the sampling frequency, the value of 10kHz was chosen, as it is a realistic value for hardware implementation, without compromising the observer performance. This led to the speed estimation results seen in Figure 7.
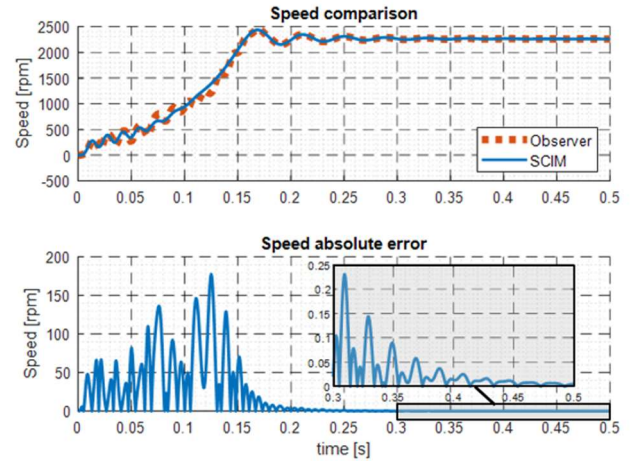

Figure 7 - Performance of Speed Estimation (DOL)

Here, we see that the estimator struggles to keep up with speed oscillations common to the transitory period of a direct on-line (DOL) startup. However, it also shows that observer converges with practically no error in steady-state, meaning it is a solid concept.

III.2.2 Soft Starter Implementation

Since the motor is part of vehicle's powertrain, DOL operation is not likely. Therefore, a as a second approach, the perfect sinusoidal system is maintained, while adding a startup with scalar command (V/f). This produces the voltage input, seen in Figure 8.
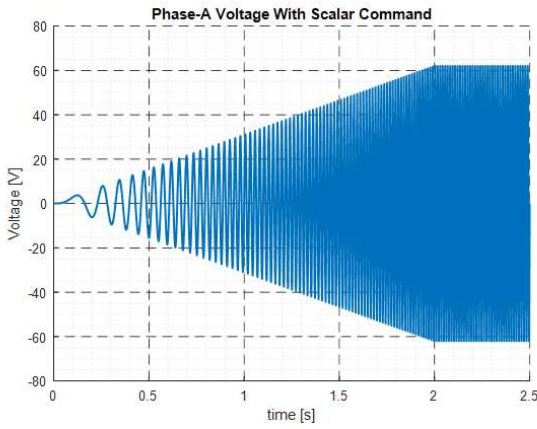
Figure 8 - Single-Phase Voltage with Scalar Command (V/f)

With this new input voltage and maintaining the simulation parameters shown in Table 1, the speed estimation results of Figure 9 are achieved.
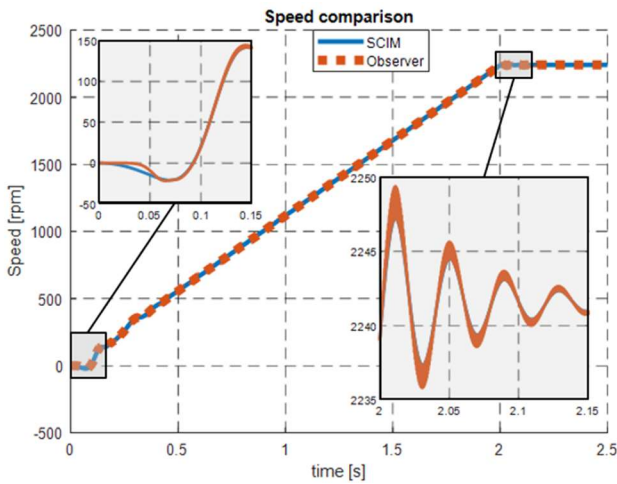

Figure 9 - Performance of Speed Estimation (V/f)

Now that the scalar command has been implemented, the observer has no issues estimating the motor's startup speed and does so with minimal error.

As for the slight distortion seen in the zoomed-in window of Figure 9, it is made up of oscillations around the true speed value, as the observer overcorrects itself repeatedly. This is due to the high values of proportional and integral gains used to speed up the observer.

III.2.3   Inverter Implementation

Finally, an inverter is added to account for the ripple present in a real-life application, thus providing a more realistic overview of the physical implementation constraints. The V/f functionality from the last section was built into the inverter, with a PWM-generator [3] slowly increasing the frequency to the nominal value. Simultaneously, the same is done for the voltage amplitude in the DC power source, maintaining the V/f ratio.

The modeled inverter is a 3-level, 3-phase PWM system. This was chosen in order to reduce the harmonic content of the input voltage, which can be seen in Figure 10.
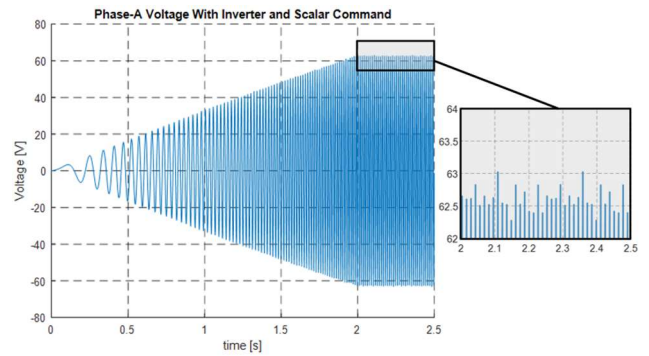

Figure 10 - Single-Phase Voltage with Inverter and Scalar Command (V/f)

This time the observer's parameters are updated to the values seen in Table 2.

Table 2 - Observer Simulation Parameters (Inverter + V/f)

Observer			
k	K_I	K_P	f_{samp}
1.1	50000	5	10 kHz

The integral gain was increased to speed up the observer's response to the fluctuations caused by the harmonics in the supply voltage, while the proportional gain was lowered to reduce the oscillatory patterns seen in the observer values. In this iteration, the value of the proportionality constant (k) was also changed to reduce the observer's response time. This leads to the results shown in Figure 11.
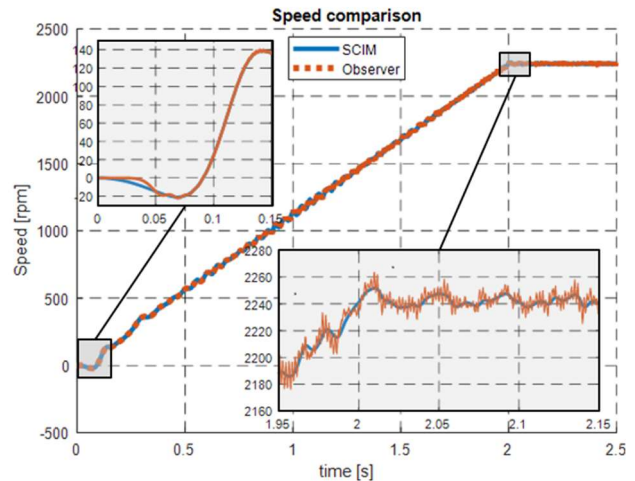

Figure 11 - Performance of Speed Estimation (INV+V/f)

The effect of the harmonics introduced by the inverter is immediately visible in the motor speed plot, as is the observer´s ability to follow its behavior.

In this case, the observer has the most trouble in steady-state. The sudden small changes in speed originating from the harmonics introduced by the inverter, cause the observer to overcompensate, leading to repeated small spikes in the error values.

Despite this the results of the model are satisfactory, so it will proceed to the physical implementation.

IV. Hardware Implementation

Two different board designs were developed to implement the speed observer, utilizing different approaches to acquire the motor's electrical data.

The first includes integrated measurement devices that sample the induction machine's stator voltage and current values. The second takes this data directly from the source, by communicating with the inverter using the CAN (Controller Area Network) protocol and sending it to a Raspberry Pi.

IV.1 External Acquisition Design

The external acquisition design uses measurement devices present on the PCB and can be divided into two main parts, the voltage acquisition and the current acquisition circuit. A render of this design is shown in Figure 12.
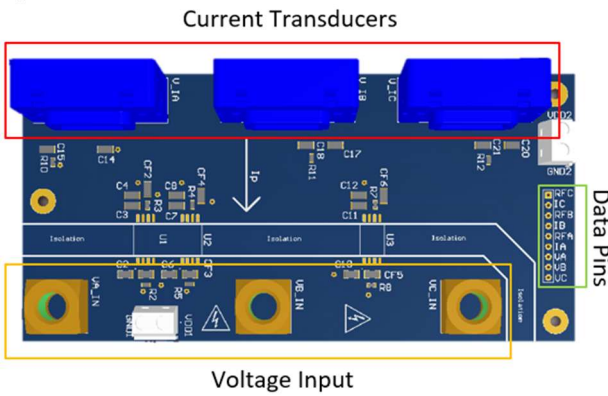

Figure 12 - 3D Render of the final PCB Design for the External Acquisition Prototype

IV.1.1 Voltage Circuit

Due to the motor's input voltage of 75V, the circuit contains three (one for each phase) AMC1301 isolated amplifiers. These offer galvanic isolation between the HV part of the board and the rest of the LV components. Additionally, voltage dividers are used to reduce the voltage to the values allowed by the OPAMP's input and low pass filters were added to remove any high frequency harmonics introduced by the inverter.

The output of the OPAMP is then filtered and sent to an Arduino for processing.

IV.1.2 Current Circuit

The current acquisition is done through HAIS 200-P current transducers (one for each phase), which also provide galvanic isolation between the motor input and the PCB.

These transducers are based on a Hall-effect measuring principle. This means a magnetic field is measured by applying a current to a thin metal strip. In the presence of a magnetic field the current flow, i.e., the flow of electrons, will be deflected, which creates a potential difference in the strip, a voltage proportional to the applied field.

In the case of a current transducer, this magnetic field was created by the cable's current flow going through its core, as shown in Figure 13.
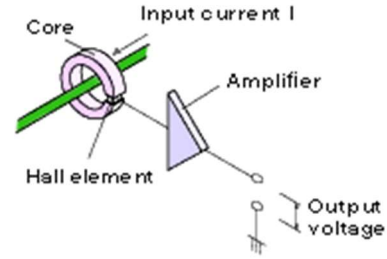

Figure 13 - Main elements of a current transducer [4]

This means the induced field is proportional to the current that is to be measured, and thus, the current can be computed from the transducer's output voltage. This conversion can be done with the expression provided by the manufacturer

$$V_{OUT} = V_{REF} \pm \left(0{,}625 \cdot \frac{I_P}{200}\right), \qquad (36)$$

where V_{REF} is a reference voltage of $2{,}5V$ and I_P is the current flowing through the sensor. These values are again sent to an Arduino where the observer model is implemented.

IV.2 CAN-HAT Design

The second design is more akin to a communication device, as it bridges the gap between the inverter's CAN interface [5] and a Raspberry Pi. Controller area network (CAN) is an electronic communication bus consisting of two wires, CAN High and CAN Low. It is a simple and low-cost solution that is widely used in the automotive industry.

Regarding the design of the prototype itself, seen in Figure 14, a choice was made early on that the PCB would be designed as a *"hat"* meaning it would have the same dimensions and subsequently be mounted on top of the Raspberry Pi, utilizing its GPIO pins for communication.
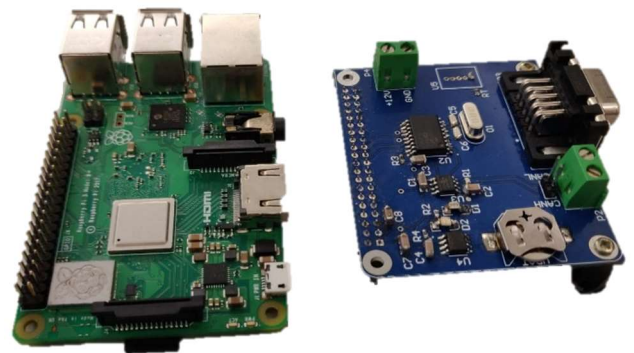

Figure 14 - Raspberry Pi3 (left) and CAN-Hat Prototype Board (right)

IV.2.1 Hardware and Circuit Design

The Block diagram in Figure 15 shows the basic principles behind this design.
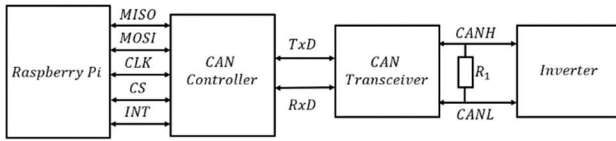

Figure 15 - Block diagram of the CAN-HAT PCB Design

The Raspberry Pi board communicates with a CAN controller through its GPIO pins, which then converts the messages according to CAN specifications, shown in Figure 16.
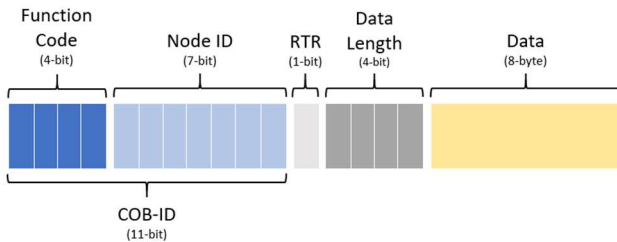

Figure 16 - CAN message layout

These are then sent to the inverter with a CAN transceiver. This process works both ways, with the inverter then sending data back to the controller, which is then decoded and read by the Raspberry Pi.

An important component to mention is the termination resistor R_1, that is placed between the CANH and CANL wires. This is a 120Ω resistor chosen according to ISO11898 [6] that must be present in all the connected nodes to avoid signal reflections.

As for the ICs, the design uses the MCP2515 as a CAN network controller. The controller converts data to and from CAN messages, allowing the user to communicate with any network device.

The bitrate of the CAN bus is set by the oscillator connected to the controller. Here, a model with a frequency of 8Mhz was chosen, resulting in a maximum bitrate of 500kbit/s. It's important to note that all nodes on a CAN bus must have the same bitrate, meaning that if another device were to be connected to the same bus, it would also have to be set to the 500kbit/s limit.

The MCP2562 CAN transceiver serves as an interface between the controller, and the physical two-wire CAN bus. This circuit includes the I/O responsible for the connection to the inverter's CAN interface, either through the two-pin headers designated P2 or a DB9 male connector. Meanwhile, the transceiver also communicates with the controller through the TXCAN (transmit) and RXCAN (receive) pins.

IV.2.2 Testing

To test the developed PCB, as well as the Raspberry Pi configuration [7] and [8], a CAN Bus Analyzer was used. This device serves as a second node in the network, allowing the user to monitor its traffic and communicate with other nodes. This testing setup is shown in Figure 17.
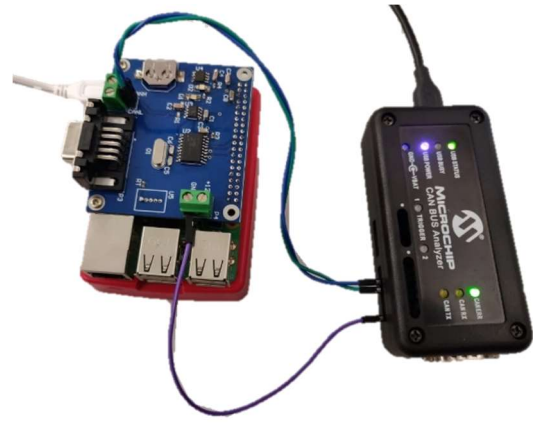

Figure 17 - CAN-Hat Prototype connected to a CAN Analyzer

What followed was a series of tests to verify the successful transmission and reception of CAN messages using the CAN-Hat prototype. For example, Figure 18, shows three identical messages sent from the CAN Analyzer. These were successfully detected by the prototype and displayed on the software terminal of the Raspberry.

Figure 18 - candump can0 output example

This result shows that all the network data is accessible to the Raspberry, meaning the CAN-Hat can fulfil its purpose of making a Raspberry Pi into a CAN bus compatible device.

V. Results

This chapter will analyze the observer's behavior in the full system simulation, including an inverter and scalar command. This is the closest scenario to the physical implementation that was initially intended. The results are divided into two sub-chapters. The first reiterates the results already presented in Figure 11, zooming in on the area with the biggest error values to further examine the observer performance. The second shows these same methods being used to analyze a scenario with a sudden load disturbance.

V.1 Constant Load

Here, the focus will be placed on the transition zone between the V/f startup ramp and steady-state operation in this scenario, as this is where the largest discrepancies between real and estimated values are found.
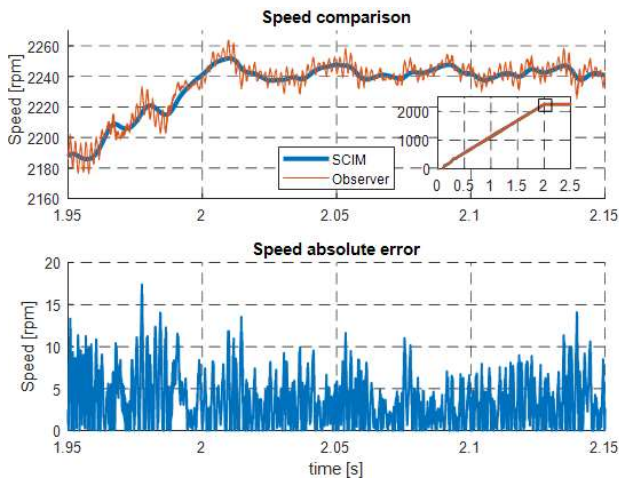
Figure 19 - Performance of Speed Estimation in the Transition to Steady State

The speed estimation found in Figure 19, show that the estimated speed oscillates around the true speed value. The estimation error in this scenario never exceeds 1%, with its highest value just before the end of the transition to steady-state. Here, it reaches an absolute value of 18Nm, which amounts to a relative error of 0.8%.

V.2   Load Disturbance

This scenario adds a disturbance in the load torque in the shape of a step that reduces the load by a value of 30Nm. This lasts for one second until the load torque returns to its original value of 65Nm. This can be seen in Figure 20, where the real and estimated torque values are compared. The observer performance is then evaluated around this disturbance zone, again using absolute error values.
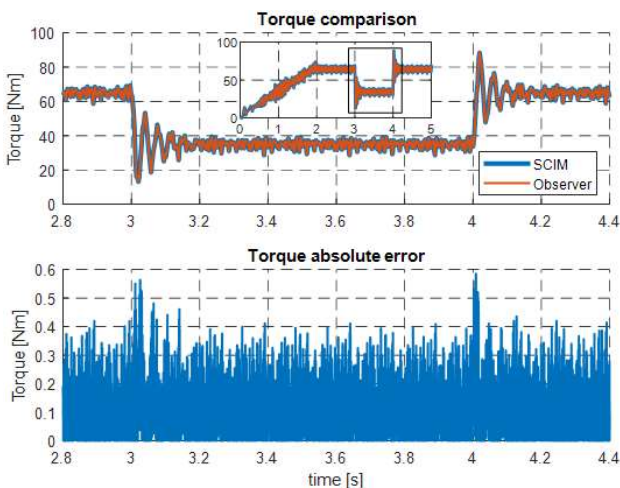

Figure 20 - Performance of Torque Estimation with a Load Disruption

The speed response to the disturbance is shown in Figure 21. Here we see that the sudden removal of about half of the load causes oscillations in the speed and that, after some time, it stabilizes at a slightly higher velocity.

The opposite effect occurs at four seconds when the load is re-applied. The speed oscillates and then returns to its original value.
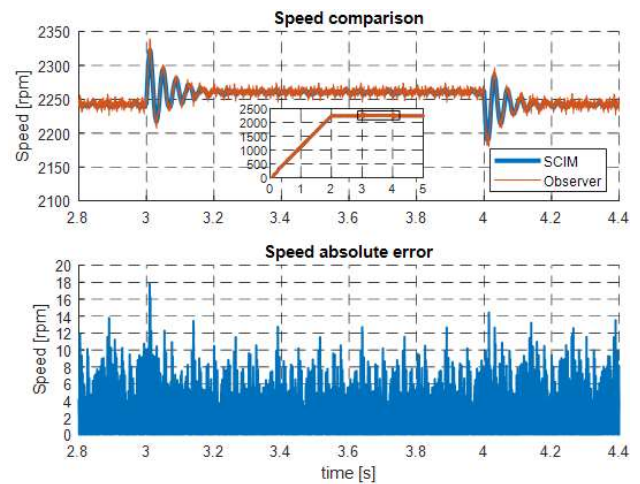

Figure 21 - Performance of Speed Estimation with a Load Disruption

As for the performance of speed estimation, we see a spike at the three-second mark where the disturbance occurs. Here the error reaches 18rpm, a 4rpm increase over the steady state error value. The error increase for the return to full load is lower, as it reaches a total error of less than 15rpm. An important observation is that the error spikes only occur at the disturbance's exact moment, immediately returning to the values seen in steady-state operation.

VI.   Conclusions

The squirrel cage induction machine's characteristics and working principles were studied in detail, including its behavior in a dynamic system. These characteristics were then converted into a stationary *dq0*-reference frame and used to create a full order speed observer.

The observer's behavior was then analyzed regarding its speed and toque estimation and compared to a simulated induction motor, developed from the machine's electrical and mechanical equations.

This led to two different electrical circuits, devised to acquire the electrical quantities feeding the VIENA's actual motor and use them as the observer's unput values.

Unfortunately, only the second design's components would be purchased due to budgetary constraints, meaning only this prototype would be completed and enter the testing phase. Here, the functionality of the CAN-Hat prototype was verified, as the Raspberry Pi was successfully made into a CAN bus compatible device.

Unfortunately, due to the ongoing global pandemic resulting in limited access to the laboratory, other systems that do not concern this master thesis but are an integral part of the vehicle's operation were not in working order, meaning the integration with the car and inverter, that was set as one of the objectives, was not possible. Nevertheless, the concept was shown to be promising and will surely be perused further in future works.

VI.1 Future Work

One aspect that could prove relevant to the improvement of observer performance is implementing an adaptive stator-resistance estimator. Since this quantity varies with temperature and significantly influences the speed estimation, the adopted approach, which consisted of measuring the stator resistance and using a constant value as the observer parameter, was not the most accurate. Such an estimator's development would be similar to that of the speed observer already described in this paper.

Some additional work would also probably arise from the actual implementation of such a prototype in the VIENA. Only then could aspects such as the real sampling frequency or the delay in the inverter's answer to data requests be considered. These factors could lead to changes to the hardware design being necessary to obtain satisfactory results from the observer. One such change that could be easily done if necessary is changing the circuit's oscillator from an 8Mhz model to 16MHz, which would essentially double the CAN bus's maximum bitrate, possibly solving any bottlenecks in the data transmission.

The observer parameters would also probably need to be readjusted to better adapt the system to the real-world conditions that it would face.

Bibliography

[1] A. E. Fitzgerald, C. J. Kingsley and U. S. D., Electric Machinery, Sixth ed., McGraw-Hill, 2003, pp. 306-356, 657-667.

[2] P. Vas, Sensorless and Direct Torque Control, Oxford University Press, 1998, pp. 263-574.

[3] J. A. Melkebeek, Electrical Machines and Drives, Springer International Publishing, 2018, pp. 117-144.

[4] KOHSHIN ELECTRIC CORPORATION, "Hall Effect Current Sensor," 2013. [Online]. Available: http://www.kohshin-ele.com/. [Accessed 15 September 2020].

[5] SEVCON, "Gen4 Applications Reference Manual Rev. 3.4".

[6] International Organization for Standardization, "Road vehicles — Controller area network (CAN) — Part 1: Data link layer and physical signalling," December 2015. [Online]. Available: https://www.iso.org.

[7] B. Tibério, "Viena: Veículo Inteligente Elétrico de Navegação Autónoma, Documentation Guide Revision 4," 2018.

[8] Raspberry Pi Foundation, "Raspberry Pi Documentation," [Online]. Available: https://www.raspberrypi.org/. [Accessed June 2020].

[9] A. Hughes, Electric Motors and Drives, Elsevier, 2006, pp. 167-304.